

Mechanosynthesized BiFeO₃ Nanoparticles with Highly Reactive Surface and Enhanced Magnetization

Klebson L. Da Silva,[§] Dirk Menzel,^{||} Armin Feldhoff,[§] Christian Kübel,[†] Michael Bruns,[#] Andrea Paesano, Jr.,[⊥] Andre Düvel,[§] Martin Wilkening,[§] Mohammad Ghafari,[†] Horst Hahn,[†] Fred J. Litterst,^{||} Paul Heitjans,[§] Klaus D. Becker,[†] and Vladimir Šepelák^{*,†,#}

[†]Institute of Nanotechnology, Karlsruhe Institute of Technology, Hermann-von-Helmholtz-Platz 1, D-76344 Eggenstein-Leopoldshafen, Germany

[‡]Institute of Physical and Theoretical Chemistry, Braunschweig University of Technology, Hans-Sommer-Strasse 10, D-38106 Braunschweig, Germany

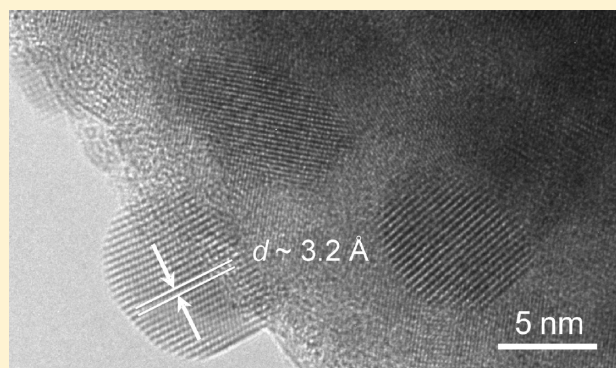
[§]Institute of Physical Chemistry and Electrochemistry, Leibniz University Hannover, Callinstrasse 3-3A, D-30167 Hannover, Germany

^{||}Institute of Condensed Matter Physics, Braunschweig University of Technology, Mendelssohnstrasse 3, D-38106 Braunschweig, Germany

[⊥]Physics Department, State University of Maringá, Av. Colombo 5790, 87020-900 Maringá, Brazil

[#]Institute for Applied Materials, Karlsruhe Institute of Technology, Hermann-von-Helmholtz-Platz 1, D-76344 Eggenstein-Leopoldshafen, Germany

ABSTRACT: A one-step synthesis of nanostructured bismuth ferrite (BiFeO₃) via mechanochemical processing of a α -Fe₂O₃/Bi₂O₃ mixture at room temperature is reported. The mechanically induced phase evolution of the mixture is followed by XRD and ⁵⁷Fe Mössbauer spectroscopy. It is shown that the mechano-synthesis of the rhombohedrally distorted perovskite BiFeO₃ phase is completed after 12 h. Compared to the traditional synthesis route, the mechanochemical process used here represents a one-step, high-yield, low-temperature, and low-cost procedure for the synthesis of BiFeO₃. High-resolution TEM and XRD studies reveal a nonuniform structure of mechano-synthesized BiFeO₃ nanoparticles consisting of a crystalline core surrounded by an amorphous surface shell. The latter is found to exhibit an extraordinarily high metastability causing a rapid crystallization of nanoparticles under irradiation with electrons. In situ high-resolution TEM observations of the crystallization clearly show that the heterogeneous processes of nucleation and growth of bismuth iron oxide crystallites are spatially confined to the amorphous surface regions. This fact provides access to the elucidation of the mechanism of mechano-synthesis. It is demonstrated that the mechano-synthesized ferrite nanoparticles exhibit a partial superparamagnetism at room temperature. Quantitative information on the short-range structure and hyperfine interactions, provided by the nuclear spectroscopic technique, is complemented by an investigation of the magnetic behavior of nanostructured BiFeO₃ on a macroscopic scale by means of SQUID technique. As a consequence of canted spins in the surface shell of nanoparticles, the mechano-synthesized BiFeO₃ exhibits an enhanced magnetization, an enhanced coercivity, and a shifted hysteresis loop.



INTRODUCTION

Multiferroics are promising materials for the design and synthesis of multifunctional materials. They are noteworthy for their unique and strong coupling of electric, magnetic, and structural order parameters, giving rise to simultaneous ferroelectricity, ferromagnetism, and ferroelasticity.¹ BiFeO₃, as a rhombohedrally distorted perovskite belonging to the space group R3c (Figure 1), is one of the most studied multiferroics possessing antiferromagnetic and ferroelectric properties at room temperature.² The material exhibits a ferroelectric Curie temperature of about 1100 K and simultaneously shows G-type antiferromagnetism below its Néel temperature of

640 K.^{2,3} Many theoretical and experimental investigations have been performed recently to characterize the properties of BiFeO₃.^{4–16} In spite of an intense study, a fundamental understanding of the structure–property correlations in BiFeO₃ is still missing. Specifically, the fundamental dependence of its magnetic behavior on the particle size is an issue of deep interest.

It is widely appreciated that the performance of multiferroics is closely related to the ways in which they are processed.

Received: October 22, 2010

Revised: February 27, 2011

The conventional solid-state (ceramic) synthesis of BiFeO_3 requires prolonged treatment at considerably high calcination temperatures,¹⁷ causing the loss of bismuth due to its high volatility. In many cases, this results in the formation of multiphase products and, consequently, in the degradation of microstructural and functional properties of the multiferroic material.^{18,19} Various wet chemistry-based routes have also been developed to synthesize nanosized multiferroic powders.^{20–22} However, most of the chemistry-based routes still involve calcinations, although at relatively lower temperatures.²³ Among the many types of preparation and processing techniques, the nonconventional mechanochemical route (mechanosynthesis) has been recognized as a powerful method for the one-step production of nanomaterials.^{24–26} In the last years, a surge of investigations in the field of mechanochemistry have clearly demonstrated that a variety of complex oxides, including ferrites,^{27–46} can be synthesized at ambient temperature directly from their precursors in the form of nanosized powders, without the need for the calcination at intermediate temperatures, thus making the process very simple and cost-effective.

In the present work, a one-step complete synthesis of nanocrystalline BiFeO_3 via mechanochemical processing of a $\alpha\text{-Fe}_2\text{O}_3/\text{Bi}_2\text{O}_3$ mixture at room temperature is reported. Although the mechanosynthesis of BiFeO_3 has already been reported by Szafraniak et al.,⁴⁷ it should be noted that in the above-mentioned paper the formation of mechanosynthesized BiFeO_3 has only been established by X-ray diffraction (XRD). As it is clearly demonstrated in the present work, solely from the XRD measurements, it is not clear whether the mechanochemical processing of the $\alpha\text{-Fe}_2\text{O}_3/\text{Bi}_2\text{O}_3$ mixture leads to the complete conversion to BiFeO_3 , even if the diffraction patterns of the milled powders exhibit typical features of the perovskite phase (see below). According to our experience,^{27–29,38,42,44,46,48,49} the simultaneous use of diffraction techniques, which are sensitivity to medium- and long-range structural order, and nuclear spectroscopic techniques such NMR and/or Mössbauer spectroscopy, which make possible observations on a local atomic scale, is indispensable in many cases to allow for a comprehensive characterization of the product of a mechanochemical reaction.

In this article, information is obtained on the short-range structure and hyperfine interactions in nanocrystalline BiFeO_3 synthesized completely in a one-step mechanochemical process. In addition to ^{57}Fe Mössbauer spectroscopy, the phase evolution during the mechanosynthesis as well as morphology and macroscopic magnetic behavior of the reaction product were monitored with comprehensive techniques including XRD, electron microscopy, and SQUID. It is demonstrated that BiFeO_3 nanoparticles possess the nonuniform core–shell configuration consisting of a crystalline inner core surrounded by an amorphous surface shell. The latter is found to be highly reactive; for the first time, the rapid kinetics of the electron beam-induced crystallization of the far-from-equilibrium surface structure of a mechanosynthesized material is monitored in situ. Moreover, an unusual property of the magnetization enhancement in nanoscale mechanosynthesized BiFeO_3 is reported.

EXPERIMENTAL SECTION

Nanocrystalline BiFeO_3 was prepared from the mixture of Bi_2O_3 (Alfa Aesar, 99.999%) and $\alpha\text{-Fe}_2\text{O}_3$ (Alfa Aesar, 99.998%) by mechanosynthesis using a high-energy planetary ball mill Pulverisette 6 (Fritsch, Germany). The starting materials were weighted in stoichiometric proportions and put into a milling chamber (250 cm³ in volume) with 22 balls (10 mm in diameter),

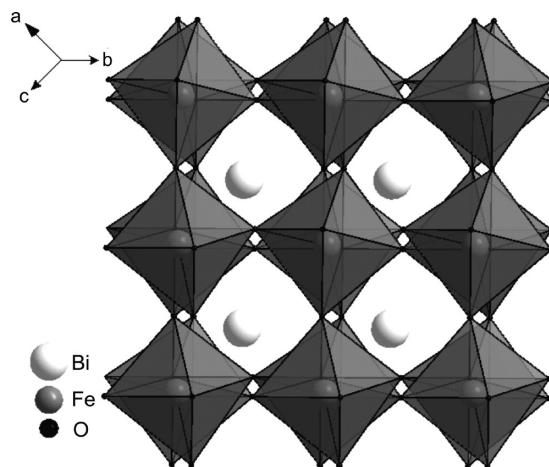


Figure 1. Rhombohedrally distorted perovskite structure of BiFeO_3 (space group $R3c$, No. 161) consisting of Fe^{3+} cations octahedrally coordinated by oxygen ions. Bi^{3+} cations are excentrically located in the cavities formed by FeO_6 octahedra.

both made of tungsten carbide. The mixtures were milled for various times t_m (up to 12 h). The ball-to-powder weight ratio was 22:1. Milling experiments were performed in air at 600 rpm.

The XRD patterns were measured using a PW 1820 X-ray diffractometer (Philips, Netherlands), operating in Bragg configuration and using $\text{Cu K}\alpha$ radiation ($\lambda = 1.54056 \text{ \AA}$). The XRD scans were collected from 20° to 80° (2θ), using a step of 0.02° and a data collection time of 5 s. The JCPDS PDF database⁵⁰ was utilized for phase identification using the STOE software. The rhombohedrally distorted perovskite structure of the mechanosynthesized BiFeO_3 was visualized using the Diamond program.⁵¹

^{57}Fe Mössbauer spectra were taken at 293 K in transmission geometry using a $^{57}\text{Co}/\text{Rh}$ γ -ray source. Recoil spectral analysis software⁵² was used for the quantitative evaluation of the Mössbauer spectra. The derived isomer shifts (IS) are given relative to IS of $\alpha\text{-Fe}$ at room temperature. The degree of conversion of the mechanochemical reaction was calculated from the Mössbauer subspectral intensities.

The morphology of powders was studied using a combined field-emission (scanning) transmission electron microscope (S)TEM (JEOL JEM-2100F) with a high-resolution pole piece that provides a point resolution better than 0.19 nm at 200 kV. An energy-dispersive X-ray (EDX) spectrometer (Oxford Instruments INCA 200 TEM) with an ultrathin window allowed for chemical analysis within grains of the mechanosynthesized material. In situ high-resolution TEM observations of the crystallization of the amorphous near-surface layers were performed using an image corrected FEI Titan 80-300 operated at 300 kV. Images were recorded under NCSI conditions using a Gatan US1000 slow-scan CCD camera. Prior to TEM investigations, powders were crushed in a mortar, dispersed in ethanol, and fixed on a copper-supported carbon grid.

Magnetic measurements were performed using a superconducting quantum interference device (SQUID) magnetometer (Quantum Design MPMS-5S). The samples were filled in a small container made of polyvinyl chloride, whose diamagnetic moment was subtracted from the measured magnetization values. Magnetic hysteresis loops were recorded at 5 K in external magnetic fields from 0 to $\pm 5 \text{ T}$. The temperature-dependent magnetic susceptibility was measured in a magnetic field of 0.1 T.

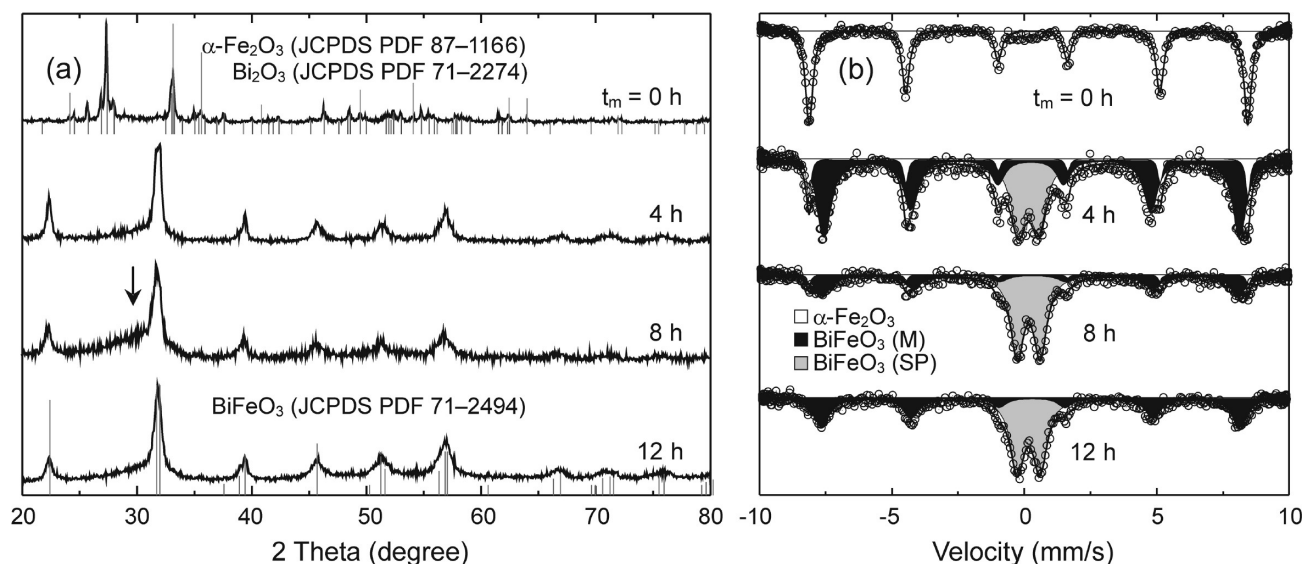


Figure 2. (a) XRD patterns and (b) ^{57}Fe Mössbauer spectra of the $\alpha\text{-Fe}_2\text{O}_3/\text{Bi}_2\text{O}_3$ mixture milled for various times. The milling times (t_m) are shown in the figure. The vertical bars indicate the positions of the diffraction peaks corresponding to the reaction precursors ($\alpha\text{-Fe}_2\text{O}_3$, Bi_2O_3) and the mechanosynthesized product phase (BiFeO_3). The arrow denotes a broad diffraction maximum in the range of about $25\text{--}35^\circ$ (2θ). (M) and (SP) denote magnetic and superparamagnetic phase of mechanosynthesized BiFeO_3 , respectively.

RESULTS AND DISCUSSION

The mechanically induced evolution of the $\alpha\text{-Fe}_2\text{O}_3/\text{Bi}_2\text{O}_3$ mixture was followed by XRD. Figure 2a shows XRD patterns of the mixture milled for various times. The XRD pattern of the starting powder is characterized by sharp peaks corresponding to the reactants $\alpha\text{-Fe}_2\text{O}_3$ (JCPDS PDF 87-1166) and Bi_2O_3 (JCPDS PDF 71-2274).⁵⁰ During the early stages of milling (for $t_m < 1$ h), XRD merely reveals a broadening of the Bragg peaks of the oxides. For milling times $1\text{ h} < t_m < 4$ h, the intensity of the XRD peaks of the educt phases gradually decreases at the expense of new diffraction peaks that correspond to the perovskite structure of BiFeO_3 (JCPDS PDF 71-2494).⁵⁰ As seen in Figure 2a, the XRD patterns of the samples milled for $t_m \geq 4$ h are dominated by the diffraction peaks of the BiFeO_3 phase; the peaks corresponding to the reactants disappeared completely after 4 h of milling. A typical feature of the XRD patterns of the mixtures milled for $4\text{ h} \leq t_m < 12$ h is that the diffraction reflections belonging to the BiFeO_3 phase are superimposed on a broad maximum in the range of about $25\text{--}35^\circ$ (2θ).

To determine the origin of this broad maximum, we performed the high-energy milling of the bulk BiFeO_3 prepared by a conventional ceramic method. It was interesting to observe that milling of BiFeO_3 is accompanied by the formation of the broad diffraction maximum in the same range (XRD patterns of the milled BiFeO_3 are not shown) as that observed in the XRD patterns of the milled $\alpha\text{-Fe}_2\text{O}_3/\text{Bi}_2\text{O}_3$ mixture. On the basis of this finding we ascribe the broad diffraction maximum in the XRD pattern of the sample milled for 12 h to an amorphous BiFeO_3 phase. It should be noted that similar diffraction features have been observed by Szafraniak et al.⁴⁷ However, the broad shape of the diffraction maximum does not allow an accurate XRD phase analysis of the milled mixtures. Therefore, the degree of conversion in the course of the present mechanochemical formation reaction will be analyzed concurrently with the discussion of Mössbauer data (see below).

To determine the phase evolution of the $\alpha\text{-Fe}_2\text{O}_3/\text{Bi}_2\text{O}_3$ mixture during high-energy milling in greater detail and to

Table 1. Parameters Obtained by Fitting the Mössbauer Spectra of the $\alpha\text{-Fe}_2\text{O}_3/\text{Bi}_2\text{O}_3$ Mixture Milled for Various Times (t_m)^a

t_m	phase	IS (mm/s)	QS (mm/s)	Γ (mm/s)	B_{hf} (T)	I (%)
0	$\alpha\text{-Fe}_2\text{O}_3$	0.348(5)	−0.08(1)	0.232	51.4(1)	100
4	$\alpha\text{-Fe}_2\text{O}_3$	0.351(5)	−0.09(1)	0.200	51.4(1)	9.7(19)
	BiFeO_3 (M)	0.376(5)	0.02(1)	0.628	48.7(1)	61.2(39)
	BiFeO_3 (SP)	0.267(5)	0.77(1)	0.706	−	29.1(12)
8	$\alpha\text{-Fe}_2\text{O}_3$	0.354(5)	−0.08(1)	0.194	51.5(1)	5.1(27)
	BiFeO_3 (M)	0.382(5)	−0.04(1)	0.728	48.7(1)	37.8(62)
	BiFeO_3 (SP)	0.277(5)	0.87(1)	0.584	−	57.0(14)
12	BiFeO_3 (M)	0.373(5)	−0.03(1)	0.682	49.0(1)	47.9(41)
	BiFeO_3 (SP)	0.269(5)	0.86(1)	0.626	−	52.1(15)

^a IS: isomer shift; QS: quadrupole splitting; Γ : Lorentzian linewidth; B_{hf} : magnetic hyperfine field; I : relative intensity; (M) and (SP): magnetic and superparamagnetic phase, respectively.

provide insight into the local structure of the formed BiFeO_3 phase, the mechanochemical reaction was also followed by ^{57}Fe Mössbauer spectroscopy. This nuclear spectroscopic method has been proven to be well suited for the investigation of the charge state, the local coordination, and the magnetic state of iron ions in mechanosynthesized materials.^{42–44,46} The room-temperature Mössbauer spectra illustrating the mechanically induced evolution of $\alpha\text{-Fe}_2\text{O}_3/\text{Bi}_2\text{O}_3$ mixtures are presented in Figure 2b. As can be seen, the spectrum of the starting mixture shows a sextet with a magnetic hyperfine field of 51.4(1) T corresponding to $\alpha\text{-Fe}_2\text{O}_3$. With increasing milling time, the sextet becomes asymmetric toward the inside of each line, slowly collapses, and is gradually replaced by a central doublet and a new broadened sextet.

The hyperfine parameters resulting from the least-squares fittings of the spectra are presented in Table 1. On the basis of these parameters, both the quadrupole split doublet and the

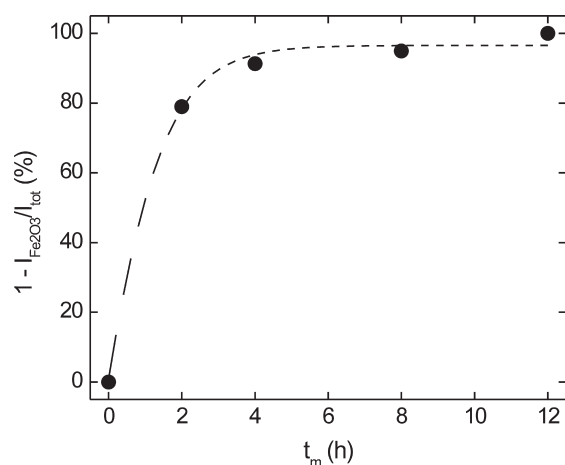


Figure 3. Time-dependent progress of reaction demonstrating the complete conversion of the educt phases during the mechanochemical synthesis of BiFeO_3 .

newly formed magnetic sextet can be assigned to ferric (Fe^{3+}) ions in octahedral coordination of oxygen ions in the perovskite structure of the mechanothesized BiFeO_3 product.⁵³ The relatively broad shape of the Mössbauer spectral lines for mechanothesized ferrite ($\Gamma \approx 0.6$ mm/s) provides clear evidence of a wide distribution of hyperfine interactions experienced by the Fe^{3+} nuclei in the material. This feature may be explained by the presence of a broad distribution of local environments around the Fe nuclei due to the deformation of FeO_6 octahedra. To elucidate the origin of the central doublet in the spectrum of mechanothesized ferrite, we should recall the effect of superparamagnetism. The latter arises if particle sizes of a material are so small that thermally induced energy fluctuations can overcome the anisotropy energy and change the direction of the magnetization of a particle from one easy axis to another.⁵⁴ In line with this, the central doublet is related to the mechanothesized ferrite particles of such small size that they behave superparamagnetic on the time scale of Mössbauer spectroscopy (about 10^{-9} to 10^{-10} s),⁵⁴ whereas the magnetic sextet component corresponds to the ferrite particles of bigger size but still in the nanoscale range; the detailed TEM analysis of the as-prepared BiFeO_3 nanoparticles is given below.

For milling times up to 8 h, the fraction of the superparamagnetic BiFeO_3 phase, estimated from Mössbauer spectra, increases from 0 to about 57% (see Table 1). On the other hand, the fraction of the magnetic BiFeO_3 phase reaches its maximum for $t_m = 4$ h. This behavior indicates that the energy transferred from the milling balls to the powder causes the nucleation of the BiFeO_3 phase already during the early stages of milling. Although the microscopic mechanism(s) and the kinetics of mechanochemical processes are scarcely elucidated,^{25,26,55,56} it can be assumed that the impact-induced local heating and high pressures (sometimes called “hot spots” or “thermal spikes”)^{56,57} involved in the high-energy milling process induce the growth of crystalline nuclei (crystallites) of the perovskite phase, reaching their maximum size for $t_m = 4$ h. This is supported by the present XRD studies; in the XRD pattern of the sample milled for 4 h, only the relatively narrow diffraction lines of BiFeO_3 are observed (see Figure 2a), corresponding to the average crystallite size of 35(3) nm. Further milling ($4 \text{ h} < t_m < 8 \text{ h}$) leads to the broadening of the XRD lines as well as to an increase of the intensity of the amorphous halo.

This reflects both the refinement of the crystallite size and the amorphization of the formed perovskite, resulting in the increase of the superparamagnetic phase at the expense of the magnetic one. It should be emphasized that, after a prolonged milling, the final size of particles/the degree of structural disorder of a treated material is a result of some equilibration between the competitive effects of the mechanically induced strains due to the ball-impact energy, which bring about the refinement of the particle size/the introduction of defects and, on the other hand, the impact-induced local heating causing the growth of particles/the structural relaxation. In the present case, the fraction of superparamagnetic and magnetic nanoparticles in the mechanothesized BiFeO_3 (with the average particle size of 20(2) nm) is about 52 and 48%, respectively. A relatively broad distribution of particle sizes (visible in TEM images below) can be a result of the heterogeneous “nucleation-and-growth” processes of the BiFeO_3 phase in the course of the mechanically induced formation reaction.

The well-resolved ^{57}Fe Mössbauer subspectra corresponding to educt ($\alpha\text{-Fe}_2\text{O}_3$) and product (BiFeO_3) phases allow an accurate determination of the degree of conversion in the course of the present mechanochemical reaction. Figure 3 illustrates the decrease in the intensity of the Mössbauer sextet corresponding to $\alpha\text{-Fe}_2\text{O}_3$, $I_{\text{Fe}_2\text{O}_3}$, relative to the total spectral intensity, I_{tot} , reflecting a gradual conversion of the reactants to the ferrite phase during milling. It is clearly seen that the mechanochemical reaction is completed after 12 h. For the samples milled for 4 and 8 h, Mössbauer spectroscopy still reveals about 10 and 5% of $\alpha\text{-Fe}_2\text{O}_3$, respectively (Table 1). Note that the presence of the educt phases in the samples milled for 4 and 8 h is not registered by XRD (see Figure 2). This gives evidence of the fact that the Mössbauer active ^{57}Fe nuclei provide a very sensitive probe for the estimation of the yield of the mechanochemical reaction. Thus, the combination of XRD and Mössbauer spectroscopy provides the full information to be gained on the progress of the mechanoynthesis.

Representative TEM micrographs of nanocrystalline mechanothesized BiFeO_3 at low and high magnifications are shown in Figure 4. It is revealed that the mechanothesized material consists of nanoparticles with a size distribution ranging from about 5 to 40 nm. Nanoparticles are found to be roughly spherical. An interesting observation is that the amorphous phase, evidenced by XRD, is confined to the near-surface layers/interfaces of BiFeO_3 nanoparticles (see Figures 4b and 5). As clearly seen, the mechanothesized material consists of crystalline regions, represented by lattice fringes in Figure 4b, and amorphous regions with the thickness of about 1 nm. It should be emphasized that the nonuniform (the so-called core-shell) configuration of nanoparticles consisting of a crystalline inner core surrounded by a structurally disordered surface shell region has also been reported for mechanothesized spinel ferrites,^{42,43} stannates,⁴⁸ and aluminates.⁵⁸ Various structural features have been found to be characteristic for a far-from-equilibrium state of the surface shell in mechanothesized nanooxides. In spinel oxide nanoparticles, for example, the nearly random cation distribution, the deformed polyhedra, and the canted spin arrangement are confined to the particle's near-surface layers with the thickness extending up to about 1 nm.^{42,43,58} Similarly, the surface structure of orthorhombic oxide nanoparticles is disordered due to broadly distorted geometry of XO_6 ($\text{X} = \text{Fe}, \text{Sn}$) octahedra.^{46,48} In the present case of the mechanothesized perovskite, the surface shell

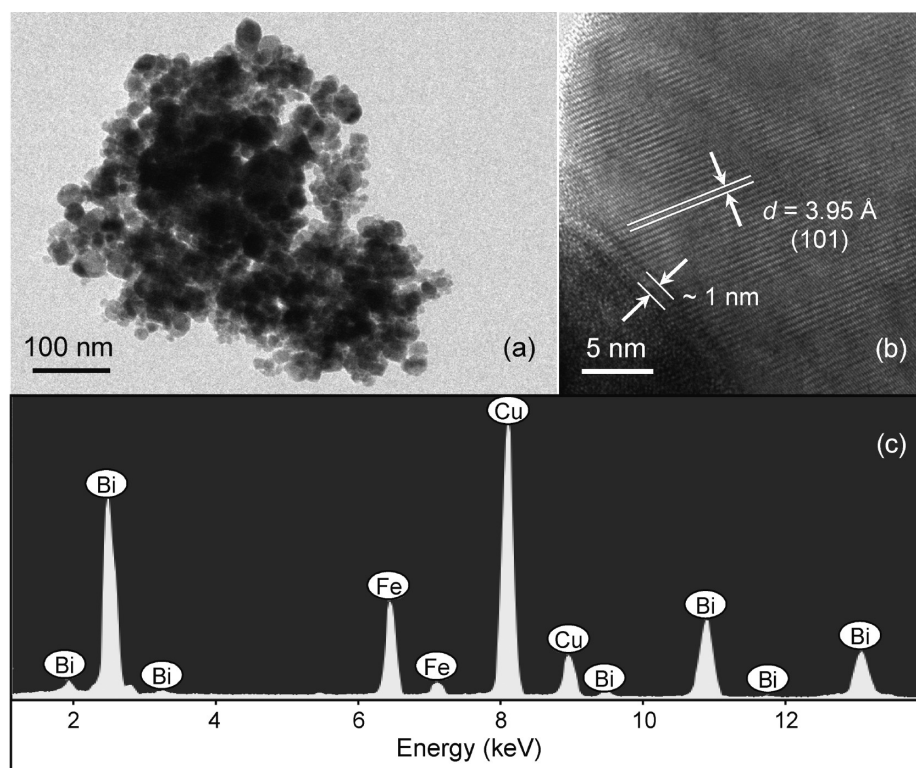


Figure 4. (a) Bright-field and (b) high-resolution TEM images of mechanosynthesized BiFeO_3 . The lattice fringes correspond to the crystallographic plane (101) ($d = 3.95 \text{ \AA}$) of the BiFeO_3 phase (JCPDS PDF 71-2494). The interface region with the thickness of about 1 nm is evident. (c) EDX spectrum of nanocrystalline mechanosynthesized BiFeO_3 .

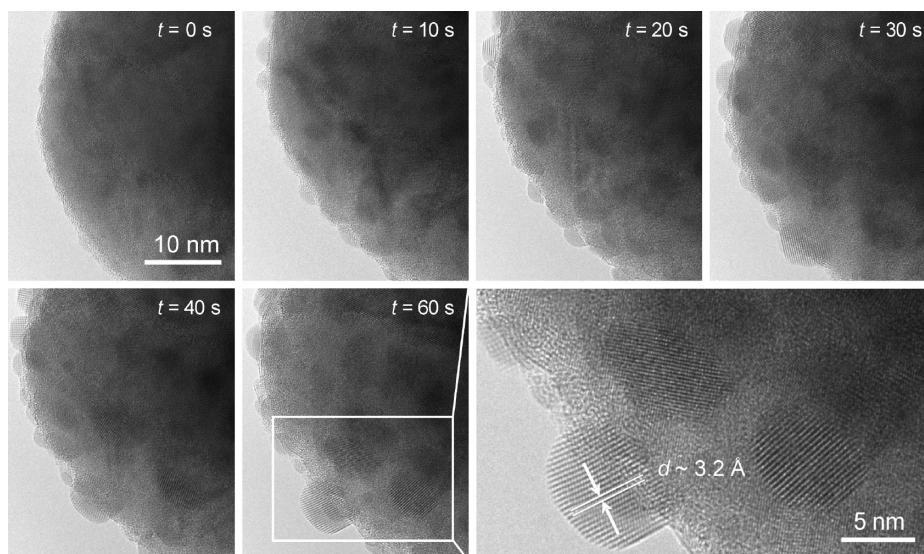


Figure 5. In situ high-resolution TEM observation of the crystallization of the amorphous near-surface layers of mechanosynthesized BiFeO_3 perovskite. An extraordinary metastability of the mechanically induced high-energy surface states manifests itself by the rapid crystallization reaction on the electron irradiation in the course of TEM investigations. The observation time (t) is shown in the figure.

regions are found to be even amorphous. On the local (short-range) scale, the deformed FeO_6 octahedra characterize the structural disorder in the near-surface layers of the as-prepared BiFeO_3 nanoparticles.

Moreover, high-resolution TEM studies reveal that the amorphous surface shell of mechanosynthesized BiFeO_3 nanoparticles

crystallizes in the course of TEM investigations! Figure 5 documents the rapid kinetics of the electron beam-induced crystallization of the far-from-equilibrium surface structure of the mechanosynthesized perovskite observed in situ. This important finding can be interpreted as a reaction of the mechanically induced high-energy surface states on the electron irradiation.

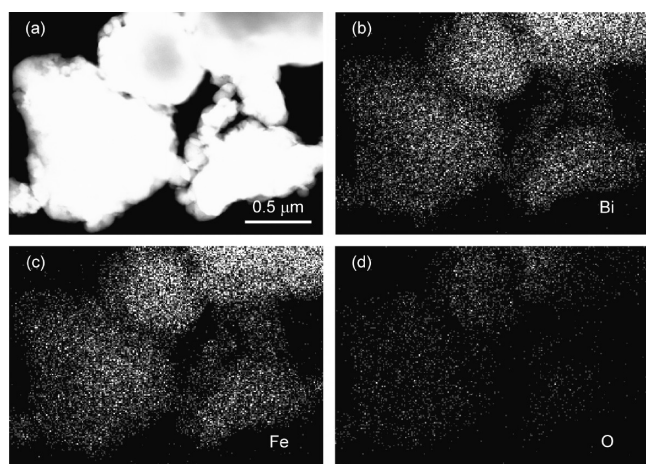


Figure 6. (a) HAADF micrograph of mechanosynthesized BiFeO_3 taken in the STEM mode. Micrographs showing distribution of the elements (b) bismuth, (c) iron, and (d) oxygen within grains of the mechanosynthesized material. Bright contrasts represent high element concentrations.

Note that very small (<5 nm) crystalline bismuth iron oxide nanoparticles observed on the surface of bigger ones (Figure 5) do not originate from the mechanosynthesis, but they are products of the crystallization of the amorphous surface layers due to their irradiation with electrons. Clearly, such a reaction of the mechanosynthesized material represents an unusual and unexpected observation; to the best of our knowledge, this is the first visual observation demonstrating both the inherent instability and a high reactivity of “fresh” mechanosynthesized surfaces. It is clearly visible that the heterogeneous processes of nucleation and growth of bismuth iron oxide crystallites are spatially confined to the amorphous surface regions. This fact can provide access to the elucidation of the mechanism of mechanosynthesis (see below).

To exclude the presence of chemical elements originating from the abrasion of the milling tools (vial and balls made of WC), we carried out further EDX, the high-angle annular dark-field (HAADF), and XPS analyses of the mechanosynthesized product. As can be seen in the representative EDX spectrum (Figure 4c), the only constituent chemical elements, Bi and Fe, were detected in the sample. Note that the spectral lines corresponding to Cu in the EDX spectrum originate from the copper-supported carbon grid.

The HAADF micrograph of the mechanosynthesized nanomaterial taken in the STEM mode (Figure 6a) shows brightness variations just due to variations in specimen thickness, as do the elemental maps that monitor the local K_α X-ray emission from bismuth, iron, and oxygen (Figure 6b–d). The HAADF analysis hints to a homogeneous distribution of the constituent elements within agglomerated grains of the mechanosynthesized material. The results of XPS investigations (spectra are not shown) support the findings of EDX and HAADF-STEM studies; Bi, Fe, and O were the only elemental components, and no impurity from the abrasion of the milling tools was detected in the sample. All these findings reveal that the mechanosynthesized ferrite is chemically homogeneous with the Bi/Fe atomic ratio being close to unity. Hereafter, we assume the ideal composition BiFeO_3 .

Although a surge of investigations in the field of mechanochemistry has resulted in the preparation of various metastable

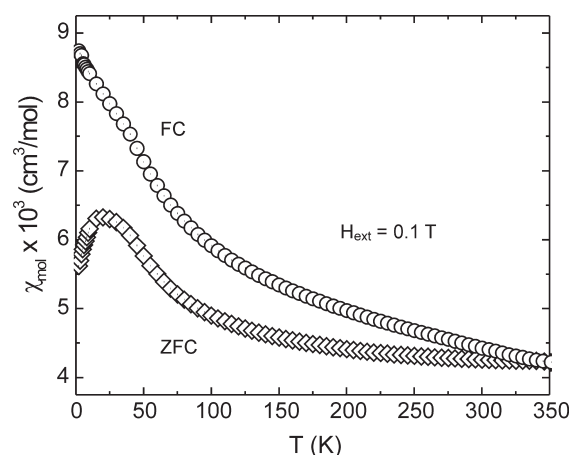


Figure 7. Temperature-dependent magnetic susceptibility (ZFC and FC) for mechanosynthesized BiFeO_3 measured under an external magnetic field of 0.1 T.

solids,^{24–26} the understanding of the basic reaction mechanisms and kinetics of mechanosynthesis has still not reached a satisfactory level, with the main reason probably being the complexity of the mechanochemical formation reactions and the shortage of systematic studies. Taking into account the present evidence of the inherently unstable and reactive mechanosynthesized surfaces (Figure 5), it may be assumed that, during the early stages of high-energy milling, the reaction precursors are mixed at the molecular level and that a new mechanosynthesized phase nucleates at interfaces between the solid reactants during the impact period. The growth mechanism of nuclei (crystallites) of the new phase could be understood as a result of the competitive effects of the impact-induced local heating and strains. The latter are accompanied by the amorphization (defects formation) of repeatedly impacted surfaces, whereas the involved “thermal spikes” cause their crystallization. Thus, based on the analogy with the electron beam-induced nucleation and growth processes, observed in the present case, we can state that the structurally disordered (amorphous) surfaces/interfaces play an essential role in the mechanically induced formation reactions; the impact-induced nucleation and growth processes of the mechanosynthesized phase are spatially confined to these high-energy regions. In this context, it should be noted that, similarly to the present case of BiFeO_3 , the mechanosynthesis of the Pb-based perovskite, $\text{Pb}(\text{Mg}_{1/3}\text{Nb}_{2/3})\text{O}_3$, has also been interpreted as the “nucleation-and-growth” process from the amorphous phase.⁵⁹

In the following, we will present the results on the macroscopic magnetic behavior of mechanosynthesized BiFeO_3 . The magnetic susceptibility of the nanomaterial was measured in the temperature range from 2 to 350 K after cooling the sample in zero applied magnetic field (ZFC) and an external magnetic field of 0.1 T (FC) (see Figure 7). Above 2 K, the increase with temperature of the ZFC curve can be ascribed to the presence of superparamagnetic particles, which give rise to a broad maximum at about 20 K. As can be seen, the FC susceptibility behaves distinctly different. The key for the discrepancy between ZFC and FC curves up to high temperatures is the observed wide distribution of particle sizes. The point at which the ZFC and FC curves start to separate (~ 333 K) is associated with the blocking temperature (T_B) of bigger particles.⁴³ Therefore, the FC susceptibility curve can be considered as a superposition of the

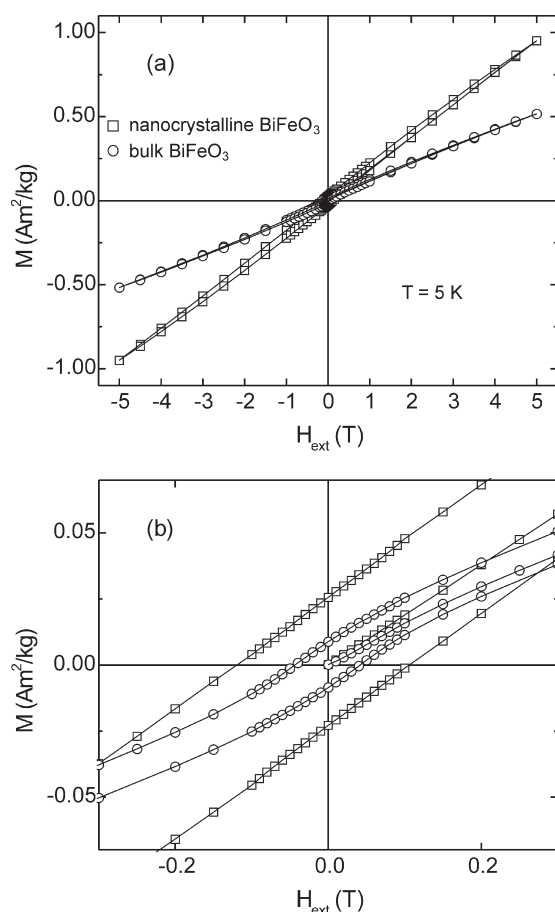


Figure 8. (a) Magnetization hysteresis loops for nanosized and bulk BiFeO₃ measured at 5 K after field cooling with $H_{\text{ext}} = 5$ T. (b) The comparison of the $M(H_{\text{ext}})$ curves for nanosized and bulk BiFeO₃ in the low-field region ($-0.3 \text{ T} < H_{\text{ext}} < 0.3 \text{ T}$) showing the shifted hysteresis loop and the enhanced coercivity for mechanosynthesized BiFeO₃.

contributions from larger bulk-like antiferromagnetic and smaller superparamagnetic BiFeO₃ nanoparticles. The latter give rise to the increase of the FC susceptibility at low temperatures. Thus, the estimated blocking temperatures of BiFeO₃ nanoparticles spread out over a wide temperature interval; although T_B of the biggest ferrite particles with diameter of about 40 nm is much higher than room temperature, T_B of the smallest (5 nm) particles is expected to be only several kelvin. The latter is supported by field-dependent magnetization measurements (Figure 8). It is clearly seen that even at very low temperature (5 K) the field-dependent magnetization is nearly linear and does not saturate at a field of 5 T. This behavior, which is dominated by the larger bulk-like antiferromagnetic BiFeO₃ particles, is superimposed by a slight hysteresis induced by the presence of canted spins in the near-surface layers of ferrite nanoparticles.^{42,43} The contribution of superparamagnetic nanoparticles is here observed as a deviation from the linearity toward saturation which, however, is small due to their tiny magnetic moment compared to the bulk-like particles.

Another interesting feature observed is that the nanoscale mechanosynthesized BiFeO₃ exhibits an enhanced magnetization in comparison with that of the bulk BiFeO₃ prepared by the conventional thermal route (Figure 8a). At the maximum field attainable ($H_{\text{ext}} = 5 \text{ T}$), the magnetization of the nanomaterial

($M = 0.952(1) \text{ Am}^2/\text{kg}$) is about 2 times larger than that of the bulk BiFeO₃ ($M = 0.517(1) \text{ Am}^2/\text{kg}$). Note that an enhanced magnetization has already been reported for nanosized BiFeO₃ prepared by various techniques, including the sol–gel method,¹ the glycine combustion synthesis process,⁹ sonochemical synthesis,⁶⁰ the high-temperature magnetic annealing,⁶¹ and the high-pressure synthesis.⁶²

To explain the origin of the enhanced magnetization in mechanosynthesized BiFeO₃, the effect of antiferromagnetism,⁶³ typical for bulk BiFeO₃, should be recalled. An antiferromagnet can be described as comprising two spin sublattices with ferromagnetic interactions within each sublattice and antiferromagnetic intersublattice interactions. Such a collinear antiparallel spin arrangement results in zero net magnetic moment due to the complete spin compensation between these two sublattices. However, as pointed out by Néel,⁶⁴ incomplete spin compensation is possible, and it becomes measurable in small antiferromagnetic systems, where the long-range antiferromagnetic order is frequently interrupted at the particle surfaces. In line with this, we attribute the enhanced magnetization of the mechanosynthesized perovskite to the canted (noncollinear) arrangement of spins in the near-surface layers of the nanoferrite. The effect of canted spins in the surface shell of BiFeO₃ nanoparticles manifests itself by the uncompensated magnetic moments of Fe³⁺ ions, enhancing the tangible contribution to the particle's overall magnetization.

In this context, it should be noted that the surface-induced magnetization has also been reported for other nanooxide systems, such as spinel ferrite nanoparticles,^{42,65} and is consistently explained in terms of the so-called *modified core–shell model*,⁶⁶ in which a competition between the effects of spin canting and site exchange of cations in the surface shell of ferrimagnetic nanoparticles plays a decisive role. According to this model, the magnetization enhancement is observed only in the case when the effect of nonequilibrium cation distribution in the shell dominates over the effect of spin canting; otherwise, a usual phenomenon like a reduction of magnetic moment may be expected for spinel ferrite nanoparticles. The present case of the mechanosynthesized perovskite clearly demonstrates that, in contrast to spinels, an enhanced magnetization in nanoferrite can also be caused by spin canting.

The presence of the canted surface spins surrounding an antiferromagnetically ordered core of the as-prepared BiFeO₃ nanoparticles is evidenced by the shift of the field-cooled hysteresis loop in both horizontal and vertical directions. As clearly shown in Figure 8b, the field-cooled hysteresis loop of the mechanosynthesized perovskite is not symmetrical about the origin but is shifted to the left (the shift ΔH_C is about 0.015 T) and toward higher magnetizations ($\Delta M \approx 0.003 \text{ Am}^2/\text{kg}$). Both horizontal and vertical shifts of the hysteresis loop are typical exchange bias features^{67,68} and are explained in terms of exchange coupling between the collinear spins in the core and the canted spins in the surface shell of nanoparticles.⁶⁹

It is also found that the nanoscale mechanosynthesized BiFeO₃ exhibits an enhanced magnetic hardness (Figure 8b); i.e., the coercive field of the mechanosynthesized material ($H_C \approx 0.113 \text{ T}$) is about 2.8 times larger than that of the bulk BiFeO₃ ($H_C \approx 40 \text{ mT}$). The enhanced coercivity may be attributed to the high volume fraction of the amorphous spin-disordered surfaces/interfaces in the nanomaterial.⁴² The magnetocrystalline anisotropy, the surface anisotropy, and the shape anisotropy may contribute to such an enhanced coercivity of ultrafine mechanosynthesized particles as well.⁶⁷

CONCLUSIONS

Nanostructured BiFeO₃ with particle sizes ranging from about 5 to 40 nm has been synthesized in a one-step mechanochemical route from the binary oxide precursors at room temperature. This nonconventional approach offers several advantages over traditional processing routes, including low-temperature solid-state reactions, fewer processing steps, homogeneity of the products, and suitability for the low-cost, large-scale production of nanopowders. In addition to the XRD method being sensitive to medium- and long-range structural order, the mechanically induced evolution of the α -Fe₂O₃/Bi₂O₃ mixture was followed by ⁵⁷Fe Mössbauer spectroscopy. The well-resolved Mössbauer spectra of the Fe-containing educt and product phases enables us to monitor the single-step mechanosynthesis route to BiFeO₃ and to accurately determine the degree of conversion of the mechanochemical reaction, reaching 100% after 12 h of milling. Furthermore, Mössbauer spectroscopy reveals the partial superparamagnetic state of the ferrite at room temperature; the fraction of superparamagnetic nanoparticles in the mechano-synthesized material is about 52%. BiFeO₃ nanoparticles are found to be roughly spherical, consisting of a crystalline inner core surrounded by an amorphous surface shell region. High-resolution TEM enable us to observe in situ the rapid kinetics of the electron beam-induced crystallization of amorphous surfaces, demonstrating their inherent instability and high reactivity. On the basis of the analogy with this observation, the mechanosynthesis of BiFeO₃ can be interpreted as the impact-induced “nucleation-and-growth” process spatially confined to the high-energy amorphous near-surface layers. The macroscopic magnetic behavior of the mechanosynthesized material (enhanced magnetization, enhanced coercivity, shifted hysteresis loop) is attributed to the effect of spin canting in the surface shell of nanoparticles.

AUTHOR INFORMATION

Corresponding Author

*Tel.: +49-721-60828929. Fax: +49-721-60826368. E-mail: vladimir.sepelak@kit.edu.

Notes

*On leave from the Slovak Academy of Sciences, Košice, Slovakia.

ACKNOWLEDGMENT

The support by the German Research Foundation (DFG) within the frame of the Priority Program “Crystalline Nonequilibrium Phases” (SPP 1415) and by the VEGA (2/0174/11) is highly acknowledged. We thank the anonymous reviewer for his valuable suggestions and comments, which helped us to improve the interpretation of the measured data and to draw out more clearly the new aspects and findings resulting from our research.

REFERENCES

- (1) Park, T.-J.; Papaefthymiou, G. C.; Viescas, A. J.; Moodenbaugh, A. R.; Wong, S. S. *Nano Lett.* **2007**, *7*, 766.
- (2) Yang, Y.; Sun, J. Y.; Zhu, K.; Liu, Y. L.; Chen, J.; Xing, X. R. *Phys. B* **2009**, *404*, 171.
- (3) Fischer, P.; Połomska, M.; Sosnowska, I.; Szymański, M. J. *Phys. C: Solid State Phys.* **1980**, *13*, 1931.
- (4) Ramesh, R.; Spaldin, N. A. *Nat. Mater.* **2007**, *6*, 21.

- (5) Wang, J.; Neaton, J. B.; Zheng, H.; Nagarajan, V.; Ogale, S. B.; Liu, B.; Viehland, D.; Vaithyanathan, V.; Schlom, D. G.; Waghmare, U. V.; Spaldin, N. A.; Rabe, K. M.; Wuttig, M.; Ramesh, R. *Science* **2003**, *299*, 1719.
- (6) Neaton, J. B.; Ederer, C.; Waghmare, U. V.; Spaldin, N. A.; Rabe, K. M. *Phys. Rev. B* **2005**, *71*, 014113.
- (7) Yang, S. Y.; Zavaliche, F.; Mohaddes-Ardabili, L.; Vaithyanathan, V.; Schlom, D. G.; Lee, Y. J.; Chu, Y. H.; Cruz, M. P.; Zhan, Q.; Zhao, T.; Ramesh, R. *Appl. Phys. Lett.* **2005**, *87*, 102903.
- (8) Palewicz, A.; Szumiata, T.; Przeniosło, R.; Sosnowska, I.; Margiolaki, I. *Solid State Commun.* **2006**, *140*, 359.
- (9) Haumont, R.; Kreisel, J.; Bouvier, P.; Hippert, F. *Phys. Rev. B* **2006**, *73*, 132101.
- (10) Yuan, G. L.; Or, S. W.; Chan, H. L. W. *J. Phys. D* **2007**, *40*, 1196.
- (11) Yang, Y.; Sun, J. Y.; Zhu, K.; Liu, Y. L.; Wan, L. J. *Appl. Phys.* **2008**, *103*, 093532.
- (12) Ramirez, M. O.; Krishnamurthi, M.; Denev, S.; Kumar, A.; Yang, S.-Y.; Chu, Y.-H.; Saiz, E.; Seidel, J.; Pyatakov, A. P.; Bush, A.; Viehland, D.; Orenstein, J.; Ramesh, R.; Gopalan, V. *Appl. Phys. Lett.* **2008**, *92*, 022511.
- (13) Jia, D.-C.; Xu, J.-H.; Ke, H.; Wang, W.; Zhou, Y. J. *Eur. Ceram. Soc.* **2009**, *29*, 3099.
- (14) Xian, T.; Yang, H.; Shen, X.; Jiang, J. L.; Wei, Z. Q.; Feng, W. J. *J. Alloy. Compd.* **2009**, *480*, 889.
- (15) Mandal, S.; Ghosh, C. K.; Sarkar, D.; Maiti, U. N.; Chattopadhyay, K. K. *Solid State Sci.* **2010**, *12*, 1803.
- (16) Selbach, S. M.; Tybell, T.; Einarsrud, M.-A.; Grande, T. J. *Solid State Chem.* **2010**, *183*, 1205.
- (17) Kothari, D.; Reddy, V. R.; Sathe, V. G.; Gupta, A.; Banerjee, A.; Awasthi, A. M. J. *Magn. Mater.* **2008**, *320*, 548.
- (18) Ghosh, S.; Dasgupta, S.; Sen, A.; Maiti, H. S. *Mater. Res. Bull.* **2005**, *40*, 2073.
- (19) Kong, L. B.; Zhang, T. S.; Ma, J.; Boey, F. *Prog. Mater. Sci.* **2008**, *53*, 207.
- (20) Selbach, S. M.; Tybell, T.; Einarsrud, M.-A.; Grande, T. *Chem. Mater.* **2007**, *19*, 6478.
- (21) Mazumder, R.; Devi, P. S.; Bhattacharya, D.; Choudhury, P.; Sen, A.; Raja, M. *Appl. Phys. Lett.* **2007**, *91*, 062510.
- (22) Fruth, V.; Tenea, E.; Gartner, M.; Anastasescu, M.; Berger, D.; Ramer, R.; Zaharescu, M. J. *Eur. Ceram. Soc.* **2007**, *27*, 937.
- (23) Maurya, D.; Thota, H.; Nalwa, K. S.; Garg, A. J. *J. Alloy. Compd.* **2009**, *477*, 780.
- (24) Kubias, B.; Fait, M. J. G.; Schlögl, R. In *Handbook of Heterogeneous Catalysis*; Ertl, G., Knözinger, H., Schüth, F., Weitkamp, J., Eds.; Wiley-VCH: Weinheim, 2008; p 571.
- (25) Avvakumov, E.; Senna, M.; Kosova, N. *Soft Mechanochemical Synthesis: A Basis for New Chemical Technologies*; Kluwer Academic Publishers: Boston, 2001.
- (26) Delogu, F.; Mulas, G. *Experimental and Theoretical Studies in Modern Mechanochemistry*; Transworld Research Network: Kerala, 2010.
- (27) Šepelák, V.; Steinike, U.; Uecker, D. C.; Wissmann, S.; Becker, K. D. J. *Solid State Chem.* **1998**, *135*, 52.
- (28) Druska, P.; Steinike, U.; Šepelák, V. J. *Solid State Chem.* **1999**, *146*, 13.
- (29) Šepelák, V.; Wissmann, S.; Becker, K. D. J. *Magn. Mater.* **1999**, *203*, 135.
- (30) Goya, G. F.; Rechenberg, H. R.; Chen, M.; Yelon, W. B. J. *Appl. Phys.* **2000**, *87*, 8005.
- (31) Kim, W.; Saito, F. *Powder Technol.* **2001**, *114*, 12.
- (32) Muroi, M.; Street, R.; McCormick, P. G.; Amighian, J. *Phys. Rev. B* **2001**, *63*, 184414.
- (33) Bhowmik, R. N.; Ranganathan, R. J. *Mater. Sci.* **2002**, *37*, 4391.
- (34) Zhou, Z. H.; Xue, J. M.; Wang, J.; Chan, H. S. O.; Yu, T.; Shen, Z. X. J. *Appl. Phys.* **2002**, *91*, 6015.
- (35) Harris, V. G.; Fatemi, D. J.; Cross, J. O.; Carpenter, E. E.; Browning, V. M.; Kirkland, J. P.; Mohan, A.; Long, G. J. J. *Appl. Phys.* **2003**, *94*, 496.
- (36) Guigue-Millot, N.; Begin-Colin, S.; Champion, Y.; Hytch, M. J.; Le Caër, G.; Perriat, P. J. *Solid State Chem.* **2003**, *170*, 30.

- (37) Bid, S.; Pradhan, S. K. *Mater. Chem. Phys.* **2003**, *82*, 27.
- (38) Šepelák, V.; Menzel, M.; Bergmann, I.; Wiebcke, M.; Krumeich, F.; Becker, K. D. *J. Magn. Magn. Mater.* **2004**, *272–276*, 1616.
- (39) Manova, E.; Kunev, B.; Paneva, D.; Mitov, I.; Petrov, L.; Estournès, C.; D'Orléans, C.; Rehspringer, J.-L.; Kurmoo, M. *Chem. Mater.* **2004**, *16*, 5689.
- (40) Padella, F.; Alvani, C.; La Barbera, A.; Ennas, G.; Liberatore, R.; Varsano, F. *Mater. Chem. Phys.* **2005**, *90*, 172.
- (41) Verdier, T.; Nachbaur, V.; Jean, M. J. *Solid State Chem.* **2005**, *178*, 3243.
- (42) Šepelák, V.; Feldhoff, A.; Heitjans, P.; Krumeich, F.; Menzel, D.; Litterst, F. J.; Bergmann, I.; Becker, K. D. *Chem. Mater.* **2006**, *18*, 3057.
- (43) Šepelák, V.; Bergmann, I.; Feldhoff, A.; Heitjans, P.; Krumeich, F.; Menzel, D.; Litterst, F. J.; Campbell, S. J.; Becker, K. D. *J. Phys. Chem. C* **2007**, *111*, 5026.
- (44) Isfahani, M. J. N.; Myndyk, M.; Šepelák, V.; Amighian, J. J. *Alloy. Compd.* **2009**, *470*, 434.
- (45) Cristóbal, A. A.; Botta, P. M.; Bercoff, P. G.; Porto López, J. M. *Mater. Res. Bull.* **2009**, *44*, 1036.
- (46) Berchmans, L. J.; Myndyk, M.; Da Silva, K. L.; Feldhoff, A.; Šubrt, J.; Heitjans, P.; Becker, K. D.; Šepelák, V. *J. Alloy. Compd.* **2010**, *500*, 68.
- (47) Szafraniak, I.; Połomska, M.; Hilczek, B.; Pietraszko, A.; Kępiński, L. *J. Eur. Ceram. Soc.* **2007**, *27*, 4399.
- (48) Šepelák, V.; Becker, K. D.; Bergmann, I.; Suzuki, S.; Indris, S.; Feldhoff, A.; Heitjans, P.; Grey, C. P. *Chem. Mater.* **2009**, *21*, 2518.
- (49) Düvel, A.; Wilkening, M.; Uecker, R.; Wegner, S.; Šepelák, V.; Heitjans, P. *Phys. Chem. Chem. Phys.* **2010**, *12*, 11251.
- (50) Joint Committee on Powder Diffraction Standards (JCPDS) Powder Diffraction File (PDF); International Centre for Diffraction Data: Newton Square, PA, 2004.
- (51) *Diamond – Crystal and Molecular Structure Visualization Software*; Crystal Impact GbR: Bonn, Germany.
- (52) Lagarec, K.; Rancourt, D. G. *Recoil – Mössbauer Spectral Analysis Software for Windows*, version 1.02; Department of Physics, University of Ottawa: Ottawa, 1998.
- (53) Menil, F. J. *Phys. Chem. Solids* **1985**, *46*, 763.
- (54) Long, G. J. *Mössbauer Spectroscopy Applied to Inorganic Chemistry*; Plenum Press: New York, 1987; Vol. 2.
- (55) Boldyrev, V. V. *Russ. Chem. Rev.* **2006**, *75*, 177.
- (56) Šepelák, V.; Menzel, M.; Becker, K. D.; Krumeich, F. J. *Phys. Chem. B* **2002**, *106*, 6672.
- (57) Heinicke, G. *Tribochemistry*; Akademie-Verlag: Berlin, 1984.
- (58) Šepelák, V.; Bergmann, I.; Indris, S.; Feldhoff, A.; Hahn, H.; Becker, K. D.; Grey, C. P.; Heitjans, P. *J. Mater. Chem.* **2011**, DOI: 10.1039/c0jm03721d.
- (59) Wang, J.; Xue, J. M.; Wan, D. M.; Gan, B. K. *J. Solid State Chem.* **2000**, *154*, 321.
- (60) Fang, L. A.; Liu, J. A.; Ju, S.; Zheng, F. G.; Dong, W.; Shen, M. R. *Appl. Phys. Lett.* **2010**, *97*, 242501.
- (61) Luo, W. J.; Wang, D. L.; Wang, F. W.; Liu, T.; Cai, J. W.; Zhang, L. Y.; Liu, Y. L. *Appl. Phys. Lett.* **2009**, *94*, 202507.
- (62) Su, W. N.; Wang, D. H.; Cao, Q. Q.; Han, Z. D.; Yin, J.; Zhang, J. R.; Du, Y. W. *Appl. Phys. Lett.* **2007**, *91*, 092905.
- (63) Néel, L. *Ann. Phys.* **1936**, *5*, 232.
- (64) Néel, L. C. R. *Acad. Sci.* **1961**, *252*, 4075.
- (65) Bhowmik, R. N.; Ranganathan, R.; Nagarajan, R.; Ghosh, B.; Kumar, S. *Phys. Rev. B* **2005**, *72*, 094405.
- (66) Šepelák, V.; Bergmann, I.; Menzel, D.; Feldhoff, A.; Heitjans, P.; Litterst, F. J.; Becker, K. D. *J. Magn. Magn. Mater.* **2007**, *316*, e764.
- (67) Nogués, J.; Sort, J.; Langlais, V.; Skumryev, V.; Surinach, S.; Muñoz, J. S.; Baró, M. D. *Phys. Rep.* **2005**, *422*, 65.
- (68) Giri, S.; Patra, M.; Majumdar, S. J. *Phys.: Condens. Matter* **2011**, *23*, 073201.
- (69) Kodama, R. H.; Berkowitz, A. E. *Phys. Rev. B* **1999**, *59*, 6321.